
Deep Kernelized Dense Geometric Matching

Johan Edstedt **Mårten Wadenbäck** **Michael Felsberg**
Computer Vision Laboratory Computer Vision Laboratory Computer Vision Laboratory
Linköping University Linköping University Linköping University
johan.edstedt@liu.se marten.wadenback@liu.se michael.felsberg@liu.se

Abstract

Geometric matching is a challenging computer vision task that involves finding correspondences between two views of a 3D scene. Dense geometric matching, *i.e.*, finding every matching pixel, is an appealing approach due to, among other things, the capacity for sub-pixel accuracy and low-texture robustness. While previous results have shown that sparse and semi-sparse methods are better suited than dense approaches for geometry estimation, we propose a novel dense method that outperforms them. We accomplish this by formulating dense global matching as a probabilistic regression task using deep kernels, in contrast to typical correlation volume processing. Furthermore, we show that replacing local correlation with warped feature stacking in the refinement stage further boosts performance. Finally, we observe that a systematic attenuation of the model confidence improves geometry estimation results. Our full approach, **Deep Kernelized Dense Geometric Matching**, sets a new state-of-the-art on the competitive HPatches, YFCC100m, MegaDepth-1500, and ScanNet-1500 geometry estimation benchmarks. We provide code for all our experiments, instructions for downloading datasets, and pretrained models, at the following repository: <https://github.com/Parskatt/dkm>

1 Introduction

Geometric matching, *i.e.*, the task of finding pixel-wise correspondences between two views of a 3D scene, is a fundamental computer vision problem with numerous important applications, including 3D reconstruction [45], SLAM [30], and visual re-localisation [27]. The task is particularly difficult, as the image pairs may exhibit extreme variations in viewpoint [20], illumination [2], day-night [43], and even season [55]. This differs from matching tasks such as optical flow, where the two views are consecutive frames from a video and changes in viewpoint and illumination are typically small.

Traditionally, geometric matching has been performed by sparse keypoint and descriptor extraction, followed by matching [25, 42]. The main issue with this approach is that reliable and repeatable keypoints are difficult to localize well in challenging scenes, leading to irrecoverable errors in estimation. To tackle this issue, semi-sparse or *detector free* methods such as LoFTR [50] and Patch2Pix [77] were introduced. These methods do not detect keypoints directly but rather perform all-to-all matching densely at a coarse level, followed by sparse match extraction and refinement. While those methods fare better in low-texture scenes, they are still fundamentally limited by the fact that the sparse matches are produced at a coarse scale. This means that their predictions exhibit grid artifacts, suffer from lack of fine level local context, and cannot describe the local geometry of the scene. We illustrate these issues in Figure 1.

The solution to all issues stated above would seem to be *dense* geometric matching, whereby *all* correspondences between the views are extracted. However, while previous dense approaches [46, 57] have achieved impressive results, they have so far failed to achieve performance rivaling that of sparse or semi-sparse methods on geometry estimation.



Figure 1: Results of our method on the MegaDepth-1500 benchmark. From left to right, support image, query image, results for the semi-sparse method LoFTR [50], results for our proposed approach **DKM**. Compared to sparse or semi-sparse approaches our approach is able to predict *every* correspondence, without any artefacts, and, in contrast to previous dense approaches, also outperform them on geometry estimation.

In this work we improve three important stages in dense matching for geometry estimation. First, during the initial global matching stage, most previous methods flatten the last two dimensions of the correlation volume and process it in 2D [28, 57], while some process the volume locally with 4D convolution [37]. The former disregards the structure of the correlation volume and forces the network to use a fixed sized resolution, while the latter uses local 4D kernels and hence is not able to use the global context. We bypass both these issues by instead viewing global matching as a probabilistic regression problem from feature to coordinate space, and show how this formulation can be solved analytically. Furthermore, we show that while the naive regression approach fails to discern multimodal matches from intermediate matches, well-chosen coordinate embeddings do not suffer those same issues, and greatly improve performance. To decode the predicted embeddings, we use a simple CNN decoder. This results in a robust and accurate coarse correspondence flow. Second, when refining the coarse correspondence flow for sub-pixel accuracy, we replace the commonly used local correlation layers [49, 57] with feature map stacking that significantly outperforms the local correlation approach. Finally, we show that a simple attenuation of the estimated confidence can improve results for geometry estimation. We provide code and instructions in the supplementary material.

Contributions Our contributions are as follows. **a)** We formulate global correlation and correspondence extraction as a feature-vector to coordinate probabilistic regression task and extend it to embedded coordinate spaces. (See Sections 3.2, 4.3) **b)** We propose warp refiners that process stacked feature maps instead of local cost-volumes, and show that it improves performance. (See Section 3.3, 4.3) **c)** We show that estimation results can be improved by attenuating the model predicted confidence. (See Sections 3.4, 4.3) **d)** By extensive experiments, we show that our approach is able to outperform all previous methods in geometry estimation, establishing dense matching as a viable alternative to the sparse paradigm. (See Section 4.2)

2 Related Work

Geometric Matching Early works focused mainly on interest point detection and local descriptors [29, 14, 75, 44], with multiple well-known improvements [25, 9, 3, 40]. More recently, learned detectors and descriptors have been increasingly popular [70, 10, 12, 36, 26, 60, 62], typically outper-

forming the hand-crafted counterparts. Additionally the matching stage itself has recently received additional attention, with NG-RANSAC [4] and SuperGlue [42] outperforming previous methods. While keypoints are useful, especially for traditional 3D reconstruction systems, they suffer from the fundamental issue that exact consistent localization between different views is impossible in practice. Furthermore, keypoint detection may completely fail in scenes with poor lighting and low-texture conditions.

One way to deal with the detector problem is semi-sparse or *detector free* geometric matching. This approach has recently received great attention with LoFTR [50] being a prominent example. These methods do not detect keypoints, but rather produce sparse correspondences by a global matching stage, followed by sparse refinement. However, due to the sparsification at the coarse level these methods exhibit grid artifacts, and lack the complete local context which dense methods achieve.

In this work we consider *dense geometric matching*. Despite its appeal, this approach has traditionally been less favored, due to its seemingly worse estimation results. The earliest learned method DGCNet [38] used the flattened global correlation volume to produce the parameters of a parametric geometric transformation. Following works [28, 57] instead produce dense warps. Neighbourhood Consensus Networks [37, 39, 77], process the 4D correlation volume with local 4D kernels, while GOCor [56] propose an internal optimization procedure on the global correlation. In contrast to previous works, we formulate the global matching problem as a probabilistic regression problem, and solve it analytically using GP regression. We additionally improve the refinement and sampling stages.

Deep Kernels / Gaussian Processes Deep kernels [67], and their associated GPs, were at first used as an alternative to SGD training in classification and regression. Some later works extend this notion to few-shot classification [32, 47, 64]. In this work, we use deep kernels to infer functions from feature-vectors to (some embedding of) spatial coordinates, which has hitherto not been explored. We additionally combine the GPs with a convolutional decoder.

Channel Decoding and Motion Coherence Decoding global matches, either as flattened correlation volumes, or in our case as predicted coordinate embeddings, can be seen as a combination of channel decoding [6, 33, 13] of embedded coordinates and robustification/local coherence [72, 65] of a vector field. Utilizing local coherence is particularly important for dense matching, since the local signal may often be intrinsically 0D or 1D, often referred to as the aperture problem [68, 61, 1].

Warp Refinement Starting from an initial solution, warp refinement seeks to improve the accuracy of the estimated warp. Early deep learning approaches [11, 16] estimated the flow coarsely in deep feature space, with flow upsampling to increase the resolution. More recently PWCNet [49], DGCNet [28], and others [57, 73, 53, 69], construct local correlation volumes in deep feature space. While they achieve good performance, they all depend on the local correlation volumes to compute offsets. In this work we instead directly stack the feature maps, which our experiments show outperforms the local correlation volume approach for geometric matching. For semi-sparse geometric matching Patch2Pix [77] refines feature patches sparsely by stacking, however their method does not use the estimated coarse warp to extract the patch.

3 Method

In the following sections we will describe our approach to estimate geometry by dense geometric matching. For an overview, see Figure 2.

3.1 Preliminaries

Consider two images I^Q, I^S (query and support) of a 3D scene. From these images we want to estimate geometry. This can, *e.g.*, be inferring the relative pose of the cameras. To accomplish this, 2D matches between the images are required. To find matches, we choose the dense geometric matching paradigm, where the task is to find all 2D matches that correspond to the same 3D point in the scene. This task can equivalently be framed as estimating a warp $W^{Q \rightarrow S}$ and a confidence mask $p(W^{Q \rightarrow S})$, which is 0 where the warp is poorly defined, *e.g.*, for occlusions or for transient objects. From this complete set of confident and non-confident matches, a subset of matches need to be sampled (without replacement) for the final estimation stage of the pipeline. Finally, a robust estimation method is used to infer the desired geometry from the sampled matches.

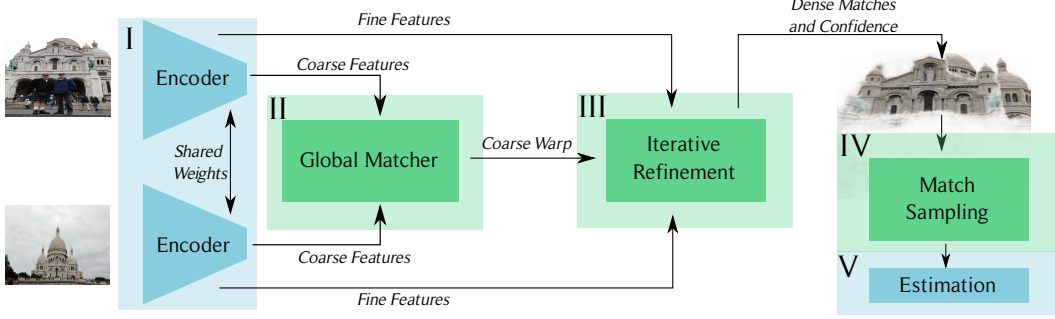


Figure 2: An overview of the geometry estimation by dense matching pipeline. **I:** In the first stage, a multiscale feature pyramid is extracted. We follow previous approaches and use ResNet-like encoders with shared weights. **II:** In the second stage coarse global matches are established. We improve this stage by viewing it as a probabilistic regression problem. We describe the regression problem and how we solve it in more detail in Section 3.2. **III:** The coarse warp is then refined. We propose a novel local-correlation free approach, which increases performance compared to previous approaches. This is detailed in Section 3.3. **IV:** Finally, for geometry estimation, a set of reliable matches need to be selected. We find that attenuation of the learned predicted confidence is beneficial. We further discuss this in Section 3.4. **V:** Once a set of matches have been selected, we use standard robust solvers for estimation as previous methods.

While the full task could be considered atomically, it is typically split it into five stages. In stage **I** feature pyramids are extracted,

$$\{\varphi_l^Q\}_{l=1}^L = F_\theta(I^Q) , \quad \{\varphi_l^S\}_{l=1}^L = F_\theta(I^S) , \quad (1)$$

where F_θ is an encoder (in our approach a ResNet variant), and $l \in \{1, \dots, L\}$ are the indices for the multiscale features (in our approach $l = 1$ corresponds to the rgb values of stride 1, and $l = L$ corresponds to deep features of stride $2^{L-1} = 32$). We will denote the coarse features as $\varphi_{\text{coarse}}^Q, \varphi_{\text{coarse}}^S$ and fine features as $\varphi_{\text{fine}}^Q, \varphi_{\text{fine}}^S$. For us the coarse features correspond to stride $\{16, 32\}$ and the fine features to $\{1, 2, 4, 8\}$.

In stage **II** we want to estimate global coarse correspondences from the deep features with a global matcher G_θ . Here potential global matches are embedded by some embedder E_θ . In most previous approaches, this is accomplished by using a semi-flattened 3+1D correlation volume

$$E_\theta(\varphi_{\text{coarse}}^Q, \varphi_{\text{coarse}}^S) = \text{Corr}(\varphi_{\text{coarse}}^Q, \varphi_{\text{coarse}}^S) \in \mathbb{R}^{H_{\text{coarse}} \times W_{\text{coarse}} \times H_{\text{coarse}} \cdot W_{\text{coarse}}} , \quad (2)$$

between the query and support image, and then process this with an embedding decoder D_θ , *i.e.*,

$$G_\theta(\varphi_{\text{coarse}}^Q, \varphi_{\text{coarse}}^S) = D_\theta(E_\theta(\varphi_{\text{coarse}}^Q, \varphi_{\text{coarse}}^S)). \quad (3)$$

If the coarse features span multiple scales, the correlation volumes are produced separately and processed for each scale in turn. However, we will instead construct E_θ through GP regression.

In stage **III** we want to refine the coarse warp of G_θ , *i.e.*

$$\begin{cases} \hat{W}^{Q \rightarrow S}, \hat{p}(\hat{W}^{Q \rightarrow S}) = R_\theta(\varphi_{\text{fine}}^Q, \varphi_{\text{fine}}^S, \hat{W}_{\text{coarse}}^{Q \rightarrow S}, \hat{p}_{\text{coarse}}(\hat{W}^{Q \rightarrow S})) , \\ \hat{W}_{\text{coarse}}^{Q \rightarrow S}, \hat{p}_{\text{coarse}}(\hat{W}^{Q \rightarrow S}) = G_\theta(\varphi_{\text{coarse}}^Q, \varphi_{\text{coarse}}^S) , \end{cases} \quad (4)$$

\hat{W} is the predicted warp, \hat{p} is the predicted confidence, and R_θ is a set of refiners. This is typically done by local correlation volume refinement. However in this work we replace the local correlation volumes with feature map stacking, which we found to improve performance.

In stage **IV**, reliable and accurate matches need to be selected for estimation of scene geometry. For sparse methods this is often done by mutual nearest neighbour matching and confidence thresholding. For dense matching, this can be done by sampling the estimated warp. We found that attenuating the estimated confidence before sampling was beneficial.

Finally, in stage **V**, a robust estimator is used to estimate geometry. We use the same RANSAC estimators as previous works.

In the following sections we will describe our approach for improving the global matcher G_θ , the warp refiners R_θ , and match sampling in more detail.

3.2 Constructing the Global Matcher G_θ

Global Matching as Regression While most previous approaches use the flattened 4D correlation volume as global match embeddings, we will instead construct the embedding as the solution to a (embedded) coordinate regression problem. We phrase this problem as finding a mapping $\varphi \rightarrow \chi$ where χ are (embeddings of) spatial coordinates in the support image. To solve any regression problem, we need a set of known mappings. Luckily, this mapping is known for the entire support grid, *i.e.*, $(\varphi_{\text{coarse}}^S, \chi_{\text{coarse}}^S)$ where each feature vector in the feature map $\varphi_{\text{coarse}}^S$ is considered as one measurement. We can choose any suitable regression framework to infer the mapping for $\varphi_{\text{coarse}}^Q$. In this work we consider GP regression.

In GP regression, the output (embedded coordinates) $\chi \in \mathbb{R}^{H \cdot W \times C}$ are considered as a collection of random variables, with the main assumption being that these are jointly Gaussian. A GP is uniquely¹ defined by its kernel which defines the covariance between outputs, and hence must be a positive-definite function to be admissible. We choose the common assumption [78] that the embedding dimensions are uncorrelated, which makes the kernel block diagonal. For the matching problem it is reasonable to assume that kernel should output a high covariance for highly correlated features, and a very low covariance for poorly correlated features, *i.e.* that similar features ought to correspond to nearby locations. One such kernel is the exponential cosine similarity kernel [22], which is defined by

$$k(\varphi, \varphi') = \exp(-\tau^{-1}) \exp\left(\tau^{-1} \frac{\langle \varphi, \varphi' \rangle}{\sqrt{\langle \varphi, \varphi \rangle \langle \varphi', \varphi' \rangle + \varepsilon}}\right). \quad (5)$$

We found this kernel to work well, but other kernels could also be considered, *e.g.*, the squared exponential kernel. We initialize $\tau = 0.2$ and let it be fixed and we let $\varepsilon = 10^{-6}$. We found that letting the kernel temperature τ be learnable had negligible effect on the performance, and that our method was robust to initializations for $\tau \in [0.1, 0.3]$.

With the standard assumption [35] that the measurements $(\varphi_{\text{coarse}}^S, \chi_{\text{coarse}}^S)$ are observed with i.i.d noise, the analytic formulae for the posterior conditioned on the support set are given by

$$\begin{cases} \mu(\varphi_{\text{coarse}}^Q | \varphi_{\text{coarse}}^S) = K_{QS} (K_{SS} + \sigma_n^2 I)^{-1} \chi_{\text{coarse}}^S \in \mathbb{R}^{H_{\text{coarse}} \cdot W_{\text{coarse}} \times C}, \\ \Sigma(\varphi_{\text{coarse}}^Q | \varphi_{\text{coarse}}^S) = K_{QQ} - K_{QS} (K_{SS} + \sigma_n^2 I)^{-1} K_{SQ} \in \mathbb{R}^{H_{\text{coarse}} \cdot W_{\text{coarse}} \times H_{\text{coarse}} \cdot W_{\text{coarse}}}, \end{cases} \quad (6)$$

where K denotes the kernel matrix, μ is the posterior mean function, σ_n is the standard deviation of the measurement noise, and Σ is the posterior covariance. We refer to Rasmussen [35] for a more complete reference on GP regression.

There are multiple ways of decoding coordinates from the posterior. We use a simple method of reshaping the predictive mean back into grid form $\mu_{\text{grid}}(\varphi_{\text{coarse}}^Q | \varphi_{\text{coarse}}^S) \in \mathbb{R}^{H_{\text{coarse}} \times W_{\text{coarse}} \times C}$ and let

$$G_\theta(\varphi_{\text{coarse}}^Q, \varphi_{\text{coarse}}^S) = D_\theta(\mu_{\text{grid}}(\varphi_{\text{coarse}}^Q | \varphi_{\text{coarse}}^S)) \quad (7)$$

where D_θ is an embedding decoder. The decoder predicts a single unconstrained coordinate in the natural grid $[-1, 1] \times [-1, 1]$, and additionally a confidence logit for the predicted validity of the match. In our implementation the decoder is constructed from the RRB and CAB blocks proposed by [71]. Full details and code for the embedding decoder are in the supplementary material.

As of yet, we have not mentioned how the spatial coordinates are embedded for regression. A naive approach would be to use an identity embedding, or a linear embedding. However, the naive approach struggles with *multi-modality*. Whenever similar features map to different coordinates, the regressive model predicts *something in between*. If this cannot be distinguished from the intermediate coordinate, there will be ambiguity in the decoding. We will call these ambiguities *metamers*, following the terminology of [48].

Coordinate Embeddings To reduce the metamer problem, we may choose an *embedding space* for our coordinates. Crucially, this embedding must be non-linear, simply due to the fact that the metamers otherwise remain.

We will consider a kind of Fourier embedding, which is a common choice [34, 51, 50, 18],

$$B_{\mathcal{F}}(x; W, b) = \cos(Wx + b), \quad (8)$$

¹With the common assumption that the mean function is 0.

where $W_{ij} \sim \mathcal{N}(0, \ell^2)$, $b_i \sim \mathcal{U}_{[0, 2\pi]}$, $i \in [1, C]$. These types of embeddings are well known to preserve multimodality [48], and possess multiple other nice properties [34, 51]. Note that neither natural coordinates, nor any affine transform thereof, behave in this way.

To demonstrate the importance of choosing an appropriate embedding, we perform an ablation experiment (Table 5) where a linear embedding is used instead of the Fourier embedding, which produces substantially worse results.

3.3 Refining the Warp with R_θ

Once the embeddings have been decoded, we use the predicted warp to align the support feature map with the query like previous work [57, 46]. However, unlike those works we do not construct local correlation volumes, but rather stack the feature maps and process them directly. We use CNNs for refinement. These output a relative offset for the estimated flow, and a logit offset for the confidence. The relative offset is added to the coarse flow, and upsampled to the next scale. The process is repeated until we reach full resolution. The process can be described recursively by

$$\hat{W}_l^{\mathcal{Q} \rightarrow \mathcal{S}}, \hat{p}_l^{\mathcal{Q} \rightarrow \mathcal{S}} = R_{\theta, l}(\varphi_l^{\mathcal{Q}}, \varphi_l^{\mathcal{S}}, \hat{W}_{l+1}^{\mathcal{Q} \rightarrow \mathcal{S}}, \hat{p}_{l+1}^{\mathcal{Q} \rightarrow \mathcal{S}}). \quad (9)$$

Each convolutional refiner consists of 8 blocks, consisting of a 5×5 depthwise separable convolution followed by batch norm [17], ReLU [31], and a 1×1 convolution. Like [23] we observe that larger depthwise kernels followed by 1×1 convolution outperforms the typical ResNet inverted block. We found it beneficial to clip the gradients between scales and use a separate regression loss (detailed in (12)) for each scale. We investigate the effect of our decision to use stacked feature maps instead of local correlation in Table 5, and find that it substantially improves performance.

3.4 Sampling Matches for geometry estimation

After dense matches have been established, scene geometry is inferred. In this work we will consider homography and 2-view relative pose estimation. For estimation, a set of putative correspondences are required, however simply selecting all matches from the output of the network is in practice infeasible since we produce $\mathcal{O}(H \cdot W)$ correspondences. A simple approach to selecting correspondences is to sample matches using the estimated match confidence as weight. This approach can be written as,

$$\{x_i^{\mathcal{Q}}, x_i^{\mathcal{S}}\}_{i=1}^N \sim \hat{p}(\hat{W}^{\mathcal{Q} \rightarrow \mathcal{S}}). \quad (10)$$

Note that in practice the sampling is done without replacement. While this approach works quite well, we found attenuating the estimated warp confidence to be beneficial for estimation. In particular we consider simple point-wise dampening of the form

$$\tilde{p} \propto \hat{p}^{1/r}, \quad r \in (0, \infty) \quad (11)$$

where we found $r \approx 2$ to work well. We plot the estimation performance on estimation benchmarks as a function of r in Figure 3.

3.5 Loss Formulation

To train our model, we use separate losses for each scale $l \in \{1, \dots, L\}$, like previous work [46, 42, 59]. While robust losses could also be considered, we found pointwise ℓ_2 distance between the predicted and reference warp to perform well. Our losses at a given layer l are

$$\mathcal{L}_{\text{warp}}(\hat{W}_l^{\mathcal{Q} \rightarrow \mathcal{S}}) = \sum p(W_l^{\mathcal{Q} \rightarrow \mathcal{S}}) \odot \|W_l^{\mathcal{Q} \rightarrow \mathcal{S}} - \hat{W}_l^{\mathcal{Q} \rightarrow \mathcal{S}}\|_2, \quad \mathcal{L}_{\text{conf}}(\hat{p}_l) = \sum p_l \log \hat{p}_l, \quad (12)$$

where the summation is done over the query grid. The reference warps can come from projected depths like in [42, 50] or from synthetic homographies, and the reference confidence p indicates, *e.g.*, covisibility or consistent depth. The confidence loss is vital for ensuring that the network is able to produce trustworthy matches. The total loss is

$$\mathcal{L} = \sum_{l=1}^L \mathcal{L}_{\text{warp}}(\hat{W}_l^{\mathcal{Q} \rightarrow \mathcal{S}}) + \lambda \mathcal{L}_{\text{conf}}(\hat{p}_l), \quad (13)$$

where $\lambda = 0.01$ is a balancing term that was chosen empirically on the training set. Like previous works [77], we set p in the fine scale loss to 0 whenever the coarse scale warp is outside a threshold distance from the reference.

4 Experiments

4.1 Training and Evaluation Details

We use two training datasets. The first is a synthetic dataset created from COCO [21], ADE20k [76], and CityScapes [7] (Non-Commercial Licenses). It is very similar to the synthetic dataset proposed by PDCNet [59] and consists of homography warps of a static background and multiple foreground objects. We additionally train on the real world dataset MegaDepth [20] (MIT License), where we generate reference warps through the dense depth maps, similarly to LoFTR [50]. We provide details and code in the supplementary material. For both datasets we train the network on images resized to a fixed resolution of 384×512 . We use a batch size of 32 and train for 250 000 gradient update steps with the AdamW [24] optimizer, with a learning rate of 10^{-4} for the decoder and refiners, and 10^{-6} for the backbone. We use weight-decay factor of 10^{-2} . We decay the learning rate with a factor 0.2 at 1/3 and 2/3 through the training. As backbone we use a ResNet50 [15] pretrained on ImageNet-1K [41]. Training takes ~ 3 days on 4 A100 GPUs. For evaluation we present the average of 5 benchmark runs, \pm the estimated standard deviation. We define the metrics used in the supplementary material. For all experiments we use the attenuation coefficient $r = 2$ for match sampling.

4.2 State of the Art Comparison

ScanNet Pose Estimation ScanNet [8] is a large scale indoor dataset, with its main challenges being low texture regions and large changes in perspective. We follow the evaluation in SuperGlue [42]. Results are presented in Table 1. Here the superiority of the dense matching paradigm for low-texture scenes becomes clear. For example, when trained on MegaDepth, our model achieves an absolute performance gain of 7% compared to LoFTR on AUC@10°.

Table 1: Pose estimation results on the ScanNet-1500 benchmark, measured in AUC (higher is better). We report results for RANSAC threshold 1 (as in PDC-Net) and 0.5 (as in LoFTR). †: Indicates a multistage or multiscale method.

Training	Method	Pose est. AUC \uparrow			Pose est. mAP \uparrow		
		@5°	@10°	@20°	@5°	@10°	@20°
<i>ScanNet</i>	SuperGlue [42] CVPR'19	16.2	33.8	51.8	-	-	-
	LoFTR [50] CVPR'21	22.1	40.8	57.6	-	-	-
	QuadTree [52] ICLR'22	24.9	44.7	61.8	-	-	-
<i>Mega + Synthetic</i>	PDCNet [59] CVPR'21	17.7	35.0	51.8	39.9	50.2	60.9
	PDCNet† [59] CVPR'21	18.7	37.0	54.0	42.9	53.1	63.3
	PDCNet+ [58] Arxiv'21	19.0	36.9	54.3	42.9	53.1	64.0
	PDCNet+† [58] Arxiv'21	20.3	39.4	57.1	45.7	56.7	67.1
	DKM t=1	23.7±0.5	43.8±0.4	61.7±0.3	51.3±0.9	61.9±0.7	72.1±0.4
	DKM t=0.5	24.8±0.5	44.4±0.3	61.9±0.1	52.2±0.6	62.1±0.4	72.1±0.2
<i>Mega</i>	LoFTR [50] CVPR'21	16.9	33.6	50.6	-	-	-
	DenseGAP [19] Arxiv'21	16.9	34.9	53.2	-	-	-
	DKM t=0.5	23.0±0.3	42.2±0.4	59.4±0.3	48.9±0.4	59.4±0.4	69.2±0.3

HPatches Homography

HPatches [2] depicts planar scenes divided in sequences, with transformations restricted to homographies. We follow the evaluation protocol of [50]. Table 2 clearly shows the superiority of our dense method, showing gains of over 5% in absolute performance.

Table 2: Homography estimation on HPatches, measured in AUC (higher is better).

Method	Pose est. AUC \uparrow		
	@3px	@5px	@10px
SuperGlue [42] CVPR'19	53.9	68.3	81.7
LoFTR [50] CVPR'21	65.9	75.6	84.6
DKM	71.2±0.5	80.2±0.3	88.1±0.2

Table 3: Pose estimation results on the YFCC100m benchmark, measured in AUC (higher is better). Here we compare our method to previous dense approaches. The top portion contains multiple pass methods, while the lower portion contains single pass methods.

	YFCC100m					
	Pose est. AUC \uparrow			Pose est. mAP \uparrow		
	@5 $^\circ$	@10 $^\circ$	@20 $^\circ$	@5 $^\circ$	@10 $^\circ$	@20 $^\circ$
RANSAC-Flow [46] ECCV'20	-	-	-	64.9	73.3	81.6
PDC-Net [59] CVPR'21	35.7	55.8	72.3	63.9	73.0	81.2
PDC-Net+ [58] Arxiv'21	37.5	58.1	74.5	67.4	76.6	84.6
OANet [74] ICCV'19	-	-	-	52.2	-	-
CoAM [66] CVPR'21	-	-	-	55.6	66.8	-
PDC-Net [59] CVPR'21	32.2	52.6	70.1	60.5	70.9	80.3
PDC-Net+ [58] Arxiv'21	34.8	55.4	72.6	63.9	73.8	82.7
DKM	40.6\pm0.3	61.2\pm0.2	77.0\pm0.1	71.0\pm0.2	79.7\pm0.1	87.0\pm0.1

YFCC100m For comparison to previous dense methods, we evaluate our approach on the pose estimation benchmark YFCC100m [54]. For comparability we use the pairs provided by [74]. Following previous methods [59] we resize the shorter side of the images to be 480. From our results in Table 3 it is clear that our method produces significantly improved results compared to all previous dense approaches.

MegaDepth-1500

We use the MegaDepth-1500 test set [50] which consists of 1500 pairs from scene 0015 and 0022. We use the same protocol as LoFTR and use a RANSAC threshold of 0.5 and resize the longer dimension of the images to 1200. Our results, presented in Table 4, show that our method is able to achieve state-of-the-art results here as well. Notably, we outperform the very recent method MatchFormer [63] which introduces a specialized attention backbone (while we use a simple ResNet).

Table 4: Pose estimation results on the Megadepth-1500 benchmark, measured in AUC (higher is better).

	Pose est. AUC \uparrow		
	@5 $^\circ$	@10 $^\circ$	@20 $^\circ$
SuperGlue [42] CVPR'19	42.2	61.2	76.0
LoFTR [50] CVPR'21	52.8	69.2	81.2
QuadTree [52] ICLR'22	53.5	70.2	82.2
MatchFormer [63] Arxiv'22	52.9	69.7	82.0
DKM	54.5\pm0.2	70.7\pm0.2	82.3\pm0.1

4.3 Ablation Study

In this section we investigate the effect of key components in our approach.

4.3.1 Architecture Design

In this ablation we evaluate the performance gains from our architectural contributions on our test split of MegaDepth, consisting of 4 scenes, and HPatches. We present our results in Table 5.

Baseline Here the global correlation volume is processed directly instead of regression. Furthermore local correlation volumes are used instead of feature stacking. This version performs poorly, achieving significantly worse results than our full method.

Naive Regression Instead of using a Fourier embedding of the coordinates, we instead use a linear embedding. We let the number of channels be the same for fairness of comparison. Notably, this version performs worse than the baseline for large thresholds. Hence it is clear that non-linear embeddings are crucial for the regression approach to succeed.

Table 5: Ablation Study.

	Dense MegaDepth PCK \uparrow			Dense HPatches PCK \uparrow		
	@1px	@3px	@5px	@1px	@3px	@5px
PDCNet [59]	-	-	-	43.9	78.5	85.8
Baseline	45.8 \pm 0.5	61.9 \pm 0.6	67.2 \pm 0.6	44.3 \pm 0.0	80.2 \pm 0.0	88.3 \pm 0.0
Naive Regression	49.7 \pm 0.8	62.2 \pm 0.9	65.9 \pm 1.0	45.7 \pm 0.0	80.5 \pm 0.0	87.9 \pm 0.0
Local Correlation	47.8 \pm 0.5	64.1 \pm 0.4	69.7 \pm 0.4	44.9 \pm 0.0	80.5 \pm 0.0	88.5 \pm 0.0
No Regression	54.2 \pm 0.7	67.7 \pm 0.8	71.6 \pm 0.7	46.5 \pm 0.0	81.5 \pm 0.0	89.0 \pm 0.0
DKM	54.6\pm0.9	68.8\pm0.9	73.0\pm0.9	46.4\pm0.0	82.2\pm0.0	89.8\pm0.0

Local Correlation Instead of stacking the warped features we use local correlation volumes for refinement. This gives significantly worse results than simple stacking. We hypothesize that correlation alone may not be enough to capture the full spectrum of feature similarity.

No Regression Here we replace regression with global correlation volume processing. This version lacks the coarse robustness provided by the GP. In particular it performs worse at PCK@5px which indicates a lack of robustness.

4.3.2 Confidence Attenuation

Here we investigate the effect of changing the attenuation coefficient r . We present results in Figure 3. A clear trend can be seen where the performance increases until $r \approx 2$. While slight improvements could be gained by choosing a specific value for each benchmark, we used $r = 2$ as to not overfit to the benchmarks.

We hypothesize that attenuating the predicted confidence leads to sampling of less certain regions which may be important in the estimation, we provide qualitative examples of the effect in the supplementary material.

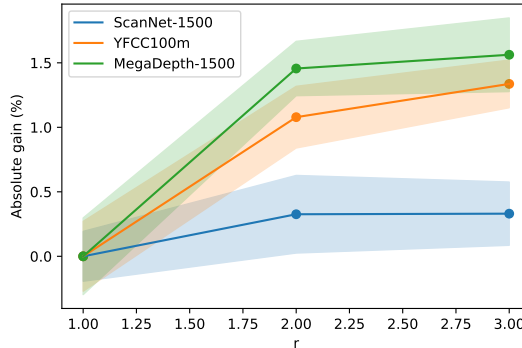


Figure 3: Effect of changing the confidence attenuation coefficient r . Absolute gain in AUC@10° plotted.

5 Conclusion

We have presented **DKM**, a dense geometric matching method that achieves state-of-the-art performance on multiple competitive geometry estimation benchmarks. We did this by improving 3 distinct stages in the matching pipeline. First we improved the global matching stage by viewing it as an embedded regression problem, yielding improvements particularly in model robustness. We additionally proposed to process warped feature maps instead of local correlation volumes in the refinement stage, yielding further gains, particularly for sub-pixel precision. Finally we investigated attenuation of model confidence for match sampling, showing that using a coefficient of $r = 2$ gave improved results in multiple benchmarks.

Limitations Our method may occasionally produce overly interpolated results near depth boundaries resulting in less accurate correspondences. This is a downside of dense methods. Additionally, small objects may sometimes be ignored by the model, which may degrade performance in geometry estimation.

Potential Negative Impact Our method is directly useful for downstream tasks such as 3D reconstruction. This means that nefarious uses of such technologies could benefit from our method. However, we are not aware of any such nefarious use cases.

Acknowledgements

This work was partially supported by the Wallenberg Artificial Intelligence, Autonomous Systems and Software Program (WASP) funded by Knut and Alice Wallenberg Foundation; and by the strategic research environment ELLIIT funded by the Swedish government. The computations were enabled by resources provided by the Swedish National Infrastructure for Computing (SNIC), partially funded by the Swedish Research Council through grant agreement no. 2018-05973.

References

- [1] Edward H Adelson and J Anthony Movshon. Phenomenal coherence of moving visual patterns. *Nature*, 300(5892):523–525, 1982.
- [2] Vassileios Balntas, Karel Lenc, Andrea Vedaldi, and Krystian Mikolajczyk. Hpatches: A benchmark and evaluation of handcrafted and learned local descriptors. In *Proceedings of the IEEE conference on computer vision and pattern recognition*, pages 5173–5182, 2017.
- [3] Herbert Bay, Tinne Tuytelaars, and Luc Van Gool. Surf: Speeded up robust features. In *European conference on computer vision*, pages 404–417. Springer, 2006.
- [4] Eric Brachmann and Carsten Rother. Neural-guided ransac: Learning where to sample model hypotheses. In *Proceedings of the IEEE/CVF International Conference on Computer Vision*, pages 4322–4331, 2019.
- [5] Alexander Buslaev, Vladimir I. Iglovikov, Eugene Khvedchenya, Alex Parinov, Mikhail Druzhinin, and Alexandr A. Kalinin. Alumentations: Fast and flexible image augmentations. *Information*, 11(2), 2020.
- [6] Fergus W Campbell and John G Robson. Application of fourier analysis to the visibility of gratings. *The Journal of physiology*, 197(3):551–566, 1968.
- [7] Marius Cordts, Mohamed Omran, Sebastian Ramos, Timo Rehfeld, Markus Enzweiler, Rodrigo Benenson, Uwe Franke, Stefan Roth, and Bernt Schiele. The cityscapes dataset for semantic urban scene understanding. In *Proceedings of the IEEE conference on computer vision and pattern recognition*, pages 3213–3223, 2016.
- [8] Angela Dai, Angel X Chang, Manolis Savva, Maciej Halber, Thomas Funkhouser, and Matthias Nießner. Scannet: Richly-annotated 3d reconstructions of indoor scenes. In *Proceedings of the IEEE conference on computer vision and pattern recognition*, pages 5828–5839, 2017.
- [9] Navneet Dalal and Bill Triggs. Histograms of oriented gradients for human detection. In *2005 IEEE computer society conference on computer vision and pattern recognition (CVPR’05)*, volume 1, pages 886–893. Ieee, 2005.
- [10] Daniel DeTone, Tomasz Malisiewicz, and Andrew Rabinovich. Superpoint: Self-supervised interest point detection and description. In *Proceedings of the IEEE conference on computer vision and pattern recognition workshops*, pages 224–236, 2018.
- [11] Alexey Dosovitskiy, Philipp Fischer, Eddy Ilg, Philip Hausser, Caner Hazirbas, Vladimir Golkov, Patrick Van Der Smagt, Daniel Cremers, and Thomas Brox. FlowNet: Learning optical flow with convolutional networks. In *Proceedings of the IEEE international conference on computer vision*, pages 2758–2766, 2015.
- [12] Mihai Dusmanu, Ignacio Rocco, Tomas Pajdla, Marc Pollefeys, Josef Sivic, Akihiko Torii, and Torsten Sattler. D2-Net: A Trainable CNN for Joint Detection and Description of Local Features. In *Proceedings of the 2019 IEEE/CVF Conference on Computer Vision and Pattern Recognition*, 2019.
- [13] M. Felsberg, P.-E. Forssén, and H. Schar. Channel smoothing: Efficient robust smoothing of low-level signal features. *IEEE Transactions on Pattern Analysis and Machine Intelligence*, 28(2), 2006.

- [14] Chris Harris, Mike Stephens, et al. A combined corner and edge detector. In *Alvey vision conference*, volume 15, pages 10–5244. Citeseer, 1988.
- [15] Kaiming He, Xiangyu Zhang, Shaoqing Ren, and Jian Sun. Deep residual learning for image recognition. In *Proceedings of the IEEE conference on computer vision and pattern recognition*, pages 770–778, 2016.
- [16] Eddy Ilg, Nikolaus Mayer, Tonmoy Saikia, Margret Keuper, Alexey Dosovitskiy, and Thomas Brox. FlowNet 2.0: Evolution of optical flow estimation with deep networks. In *Proceedings of the IEEE conference on computer vision and pattern recognition*, pages 2462–2470, 2017.
- [17] Sergey Ioffe and Christian Szegedy. Batch normalization: Accelerating deep network training by reducing internal covariate shift. In *International conference on machine learning*, pages 448–456. PMLR, 2015.
- [18] Wei Jiang, Eduard Trulls, Jan Hosang, Andrea Tagliasacchi, and Kwang Moo Yi. COTR: Correspondence Transformer for Matching Across Images. In *ICCV*, 2021.
- [19] Zhengfei Kuang, Jiaman Li, Mingming He, Tong Wang, and Yajie Zhao. Densegap: Graph-structured dense correspondence learning with anchor points. *arXiv preprint arXiv:2112.06910*, 2021.
- [20] Zhengqi Li and Noah Snavely. Megadepth: Learning single-view depth prediction from internet photos. In *Proceedings of the IEEE Conference on Computer Vision and Pattern Recognition*, pages 2041–2050, 2018.
- [21] Tsung-Yi Lin, Michael Maire, Serge Belongie, James Hays, Pietro Perona, Deva Ramanan, Piotr Dollár, and C Lawrence Zitnick. Microsoft coco: Common objects in context. In *European conference on computer vision*, pages 740–755. Springer, 2014.
- [22] Ze Liu, Han Hu, Yutong Lin, Zhuliang Yao, Zhenda Xie, Yixuan Wei, Jia Ning, Yue Cao, Zheng Zhang, Li Dong, et al. Swin transformer v2: Scaling up capacity and resolution. *arXiv preprint arXiv:2111.09883*, 2021.
- [23] Zhuang Liu, Hanzi Mao, Chao-Yuan Wu, Christoph Feichtenhofer, Trevor Darrell, and Saining Xie. A convnet for the 2020s. *arXiv preprint arXiv:2201.03545*, 2022.
- [24] Ilya Loshchilov and Frank Hutter. Decoupled weight decay regularization. In *International Conference on Learning Representations*, 2019.
- [25] David G Lowe. Distinctive image features from scale-invariant keypoints. *International journal of computer vision*, 60(2):91–110, 2004.
- [26] Zixin Luo, Tianwei Shen, Lei Zhou, Jiahui Zhang, Yao Yao, Shiwei Li, Tian Fang, and Long Quan. Contextdesc: Local descriptor augmentation with cross-modality context. In *Proceedings of the IEEE/CVF Conference on Computer Vision and Pattern Recognition*, pages 2527–2536, 2019.
- [27] Simon Lynen, Bernhard Zeisl, Dror Aiger, Michael Bosse, Joel Hesch, Marc Pollefeys, Roland Siegwart, and Torsten Sattler. Large-scale, real-time visual–inertial localization revisited. *The International Journal of Robotics Research*, 39(9):1061–1084, 2020.
- [28] Iaroslav Melekhov, Aleksei Tiulpin, Torsten Sattler, Marc Pollefeys, Esa Rahtu, and Juho Kannala. Dgc-net: Dense geometric correspondence network. In *2019 IEEE Winter Conference on Applications of Computer Vision (WACV)*, pages 1034–1042. IEEE, 2019.
- [29] Hans P Moravec. Rover visual obstacle avoidance. In *IJCAI*, volume 81, pages 785–790, 1981.
- [30] Raul Mur-Artal, Jose Maria Martinez Montiel, and Juan D Tardos. Orb-slam: a versatile and accurate monocular slam system. *IEEE transactions on robotics*, 31(5):1147–1163, 2015.
- [31] Vinod Nair and Geoffrey E Hinton. Rectified linear units improve restricted boltzmann machines. In *ICML*, 2010.

- [32] Massimiliano Patacchiola, Jack Turner, Elliot J. Crowley, and Amos Storkey. Bayesian meta-learning for the few-shot setting via deep kernels. In *Advances in Neural Information Processing Systems*, 2020.
- [33] Alexandre Pouget, Peter Dayan, and Richard Zemel. Information processing with population codes. *Nature Reviews Neuroscience*, 1(2):125–132, 2000.
- [34] Ali Rahimi and Benjamin Recht. Random features for large-scale kernel machines. In *Proceedings of the 20th International Conference on Neural Information Processing Systems, NIPS’07*, page 1177–1184, 2007.
- [35] Carl Edward Rasmussen and Christopher K. I. Williams. *Gaussian Processes for Machine Learning (Adaptive Computation and Machine Learning)*. The MIT Press, 2005.
- [36] Jerome Revaud, Cesar De Souza, Martin Humenberger, and Philippe Weinzaepfel. R2d2: Reliable and repeatable detector and descriptor. *Advances in neural information processing systems*, 32:12405–12415, 2019.
- [37] I. Rocco, M. Cimpoi, R. Arandjelović, A. Torii, T. Pajdla, and J. Sivic. Neighbourhood consensus networks. In *Proceedings of the 32nd Conference on Neural Information Processing Systems*, 2018.
- [38] Ignacio Rocco, Relja Arandjelovic, and Josef Sivic. Convolutional neural network architecture for geometric matching. In *Proceedings of the IEEE conference on computer vision and pattern recognition*, pages 6148–6157, 2017.
- [39] Ignacio Rocco, Relja Arandjelović, and Josef Sivic. Efficient neighbourhood consensus networks via submanifold sparse convolutions. In *European Conference on Computer Vision*, pages 605–621. Springer, 2020.
- [40] Ethan Rublee, Vincent Rabaud, Kurt Konolige, and Gary Bradski. Orb: An efficient alternative to sift or surf. In *2011 International conference on computer vision*, pages 2564–2571. Ieee, 2011.
- [41] Olga Russakovsky, Jia Deng, Hao Su, Jonathan Krause, Sanjeev Satheesh, Sean Ma, Zhiheng Huang, Andrej Karpathy, Aditya Khosla, Michael Bernstein, et al. Imagenet large scale visual recognition challenge. *International journal of computer vision*, 115(3):211–252, 2015.
- [42] Paul-Edouard Sarlin, Daniel DeTone, Tomasz Malisiewicz, and Andrew Rabinovich. Superglue: Learning feature matching with graph neural networks. In *Proceedings of the IEEE/CVF conference on computer vision and pattern recognition*, pages 4938–4947, 2020.
- [43] Torsten Sattler, Will Maddern, Carl Toft, Akihiko Torii, Lars Hammarstrand, Erik Stenborg, Daniel Safari, Masatoshi Okutomi, Marc Pollefeys, Josef Sivic, et al. Benchmarking 6dof outdoor visual localization in changing conditions. In *Proceedings of the IEEE Conference on Computer Vision and Pattern Recognition*, pages 8601–8610, 2018.
- [44] Cordelia Schmid and Roger Mohr. Local grayvalue invariants for image retrieval. *IEEE transactions on pattern analysis and machine intelligence*, 19(5):530–535, 1997.
- [45] Johannes L Schonberger and Jan-Michael Frahm. Structure-from-motion revisited. In *Proceedings of the IEEE conference on computer vision and pattern recognition*, pages 4104–4113, 2016.
- [46] Xi Shen, François Darmon, Alexei A Efros, and Mathieu Aubry. Ransac-flow: generic two-stage image alignment. In *Computer Vision—ECCV 2020: 16th European Conference, Glasgow, UK, August 23–28, 2020, Proceedings, Part IV 16*, pages 618–637. Springer, 2020.
- [47] Jake Snell and Richard Zemel. Bayesian few-shot classification with one-vs-each pólya-gamma augmented gaussian processes. In *International Conference on Learning Representations*, 2021.
- [48] Herman P Snippe and Jan J Koenderink. Discrimination thresholds for channel-coded systems. *Biological cybernetics*, 66(6):543–551, 1992.

- [49] Deqing Sun, Xiaodong Yang, Ming-Yu Liu, and Jan Kautz. Pwc-net: Cnns for optical flow using pyramid, warping, and cost volume. In *Proceedings of the IEEE conference on computer vision and pattern recognition*, pages 8934–8943, 2018.
- [50] Jiaming Sun, Zehong Shen, Yuang Wang, Hujun Bao, and Xiaowei Zhou. Loftr: Detector-free local feature matching with transformers. In *Proceedings of the IEEE/CVF Conference on Computer Vision and Pattern Recognition*, pages 8922–8931, 2021.
- [51] Matthew Tancik, Pratul P Srinivasan, Ben Mildenhall, Sara Fridovich-Keil, Nithin Raghavan, Utkarsh Singhal, Ravi Ramamoorthi, Jonathan T Barron, and Ren Ng. Fourier features let networks learn high frequency functions in low dimensional domains. In *Advances in Neural Information Processing Systems 33: Annual Conference on Neural Information Processing Systems 2020, NeurIPS 2020, December 6-12, 2020, virtual*.
- [52] Shitao Tang, Jiahui Zhang, Siyu Zhu, and Ping Tan. Quadtree attention for vision transformers. In *International Conference on Learning Representations*, 2022.
- [53] Zachary Teed and Jia Deng. Raft: Recurrent all-pairs field transforms for optical flow. In *European conference on computer vision*, pages 402–419. Springer, 2020.
- [54] Bart Thomee, David A Shamma, Gerald Friedland, Benjamin Elizalde, Karl Ni, Douglas Poland, Damian Borth, and Li-Jia Li. Yfcc100m: The new data in multimedia research. *Communications of the ACM*, 59(2):64–73, 2016.
- [55] Carl Toft, Will Maddern, Akihiko Torii, Lars Hammarstrand, Erik Stenborg, Daniel Safari, Masatoshi Okutomi, Marc Pollefeys, Josef Sivic, Tomas Pajdla, et al. Long-term visual localization revisited. *IEEE Transactions on Pattern Analysis and Machine Intelligence*, 2020.
- [56] Prune Truong, Martin Danelljan, Luc V Gool, and Radu Timofte. Gocor: Bringing globally optimized correspondence volumes into your neural network. *Advances in Neural Information Processing Systems*, 33, 2020.
- [57] Prune Truong, Martin Danelljan, and Radu Timofte. Glu-net: Global-local universal network for dense flow and correspondences. In *Proceedings of the IEEE/CVF conference on computer vision and pattern recognition*, pages 6258–6268, 2020.
- [58] Prune Truong, Martin Danelljan, Radu Timofte, and Luc Van Gool. Pdc-net+: Enhanced probabilistic dense correspondence network. *arXiv preprint arXiv:2109.13912*, 2021.
- [59] Prune Truong, Martin Danelljan, Luc Van Gool, and Radu Timofte. Learning accurate dense correspondences and when to trust them. In *Proceedings of the IEEE/CVF Conference on Computer Vision and Pattern Recognition*, pages 5714–5724, 2021.
- [60] Michal J. Tyszkiewicz, Pascal Fua, and Eduard Trulls. DISK: learning local features with policy gradient. In *NeurIPS*, 2020.
- [61] Hans Wallach. Über visuell wahrgenommene bewegungsrichtung. *Psychologische Forschung*, 20(1):325–380, 1935.
- [62] Qianqian Wang, Xiaowei Zhou, Bharath Hariharan, and Noah Snavely. Learning feature descriptors using camera pose supervision. In *Proc. European Conference on Computer Vision (ECCV)*, 2020.
- [63] Qing Wang, Jiaming Zhang, Kailun Yang, Kunyu Peng, and Rainer Stiefelhagen. Matchformer: Interleaving attention in transformers for feature matching. *arXiv preprint arXiv:2203.09645*, 2022.
- [64] Ze Wang, Zichen Miao, Xiantong Zhen, and Qiang Qiu. Learning to learn dense gaussian processes for few-shot learning. *Advances in Neural Information Processing Systems*, 34, 2021.
- [65] Yar Weiss and Edward H Adelson. Slow and smooth: A bayesian theory for the combination of local motion signals in human vision. *MIT AI Memo 1624*, 1998.

- [66] Olivia Wiles, Sebastien Ehrhardt, and Andrew Zisserman. Co-attention for conditioned image matching. In *Proceedings of the IEEE/CVF Conference on Computer Vision and Pattern Recognition*, pages 15920–15929, 2021.
- [67] Andrew Gordon Wilson, Zhiting Hu, Ruslan Salakhutdinov, and Eric P Xing. Deep kernel learning. In *Artificial intelligence and statistics*, pages 370–378. PMLR, 2016.
- [68] Adolf Wohlgenuth. *On the after-effect of seen movement*. Number 1-2. University Press, 1911.
- [69] Haofei Xu, Jing Zhang, Jianfei Cai, Hamid Reza Tofighi, and Dacheng Tao. Gmflow: Learning optical flow via global matching. *Proceedings of the IEEE/CVF Conference on Computer Vision and Pattern Recognition*, 2022.
- [70] Kwang Moo Yi, Eduard Trulls, Vincent Lepetit, and Pascal Fua. Lift: Learned invariant feature transform. In *European conference on computer vision*, pages 467–483. Springer, 2016.
- [71] Changqian Yu, Jingbo Wang, Chao Peng, Changxin Gao, Gang Yu, and Nong Sang. Learning a discriminative feature network for semantic segmentation. In *Proceedings of the IEEE conference on computer vision and pattern recognition*, pages 1857–1866, 2018.
- [72] Alan L Yuille and Norberto M Grzywacz. A computational theory for the perception of coherent visual motion. *Nature*, 333(6168):71–74, 1988.
- [73] Feihu Zhang, Oliver J. Woodford, Victor Adrian Prisacariu, and Philip H.S. Torr. Separable flow: Learning motion cost volumes for optical flow estimation. In *Proceedings of the IEEE/CVF International Conference on Computer Vision (ICCV)*, pages 10807–10817, 2021.
- [74] Jiahui Zhang, Dawei Sun, Zixin Luo, Anbang Yao, Lei Zhou, Tianwei Shen, Yurong Chen, Long Quan, and Hongen Liao. Learning two-view correspondences and geometry using order-aware network. *International Conference on Computer Vision (ICCV)*, 2019.
- [75] Zhengyou Zhang, Rachid Deriche, Olivier Faugeras, and Quang-Tuan Luong. A robust technique for matching two uncalibrated images through the recovery of the unknown epipolar geometry. *Artificial intelligence*, 78(1-2):87–119, 1995.
- [76] Bolei Zhou, Hang Zhao, Xavier Puig, Sanja Fidler, Adela Barriuso, and Antonio Torralba. Scene parsing through ade20k dataset. In *Proceedings of the IEEE conference on computer vision and pattern recognition*, pages 633–641, 2017.
- [77] Qunjie Zhou, Torsten Sattler, and Laura Leal-Taixe. Patch2pix: Epipolar-guided pixel-level correspondences. In *Proceedings of the IEEE/CVF Conference on Computer Vision and Pattern Recognition*, pages 4669–4678, 2021.
- [78] Mauricio A. Álvarez, Lorenzo Rosasco, and Neil D. Lawrence. Kernels for vector-valued functions: A review. *Foundations and Trends® in Machine Learning*, 4(3):195–266, 2012.

A Appendix

A.1 Additional Qualitative Examples

YFCC100m We provide qualitative examples in Figure 4. Our approach is robust to large changes in viewpoint, and is able to tackle very challenging image pairs.

ScanNet-1500 The ScanNet-1500 benchmark poses unique challenges such as extreme lack of texture and motion blur. We demonstrate qualitative results of DKM in Figure 5. We see that our model is able to generalize to these sequences as well. The model is notably more uncertain for ScanNet compared to YFCC100m. We attribute this to the lack of texture to support certain predictions.

Multimodality In the main paper we claimed that Fourier embeddings enable multimodal regression. Here we show that this is indeed the case in trained models by plotting the cosine similarity between the GP posterior mean and the Fourier embeddings for a specific pixel in the query image. This is



Figure 4: Qualitative examples of DKM applied to the YFCC100m benchmark.

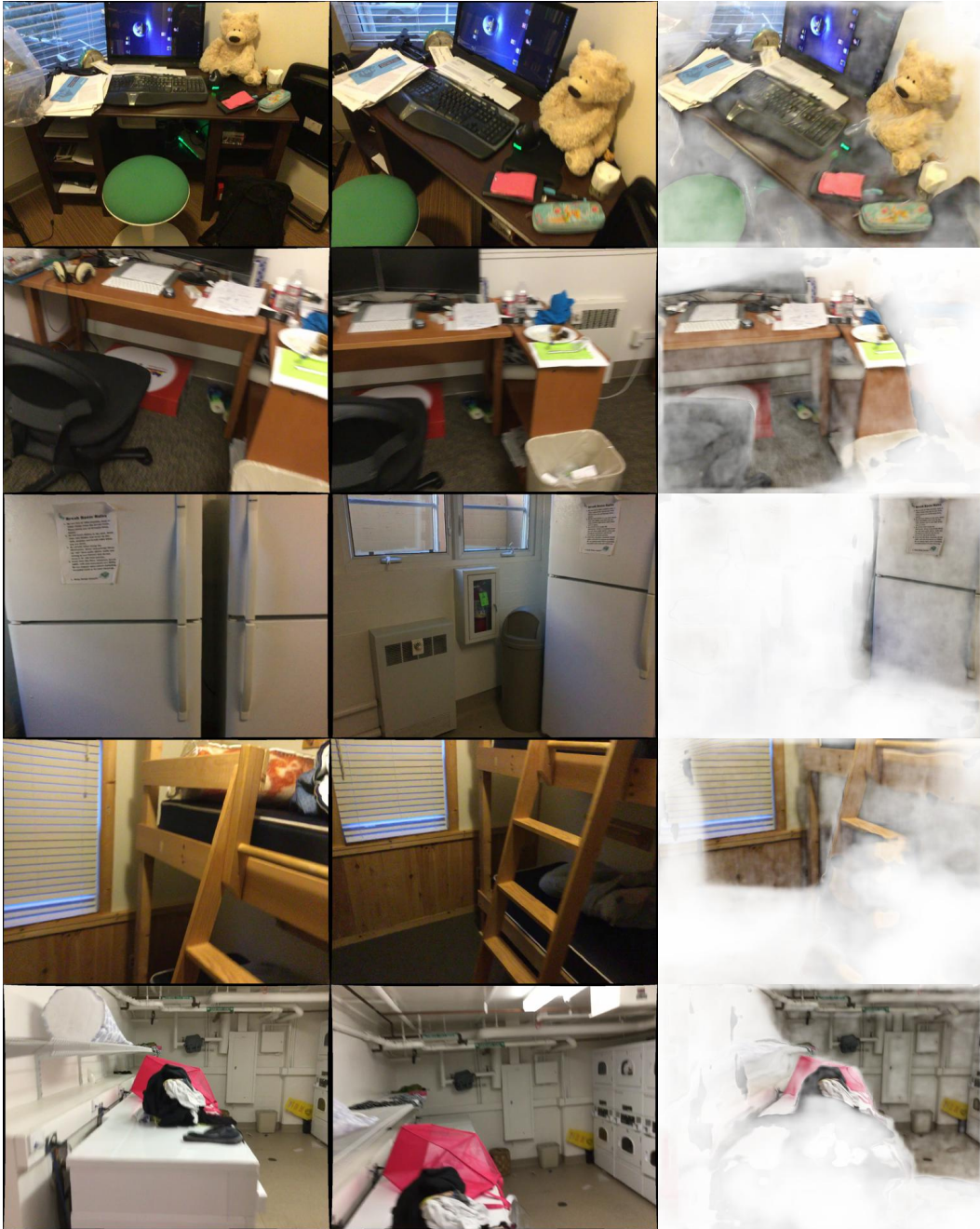


Figure 5: Qualitative examples of DKM applied to the ScanNet benchmark.

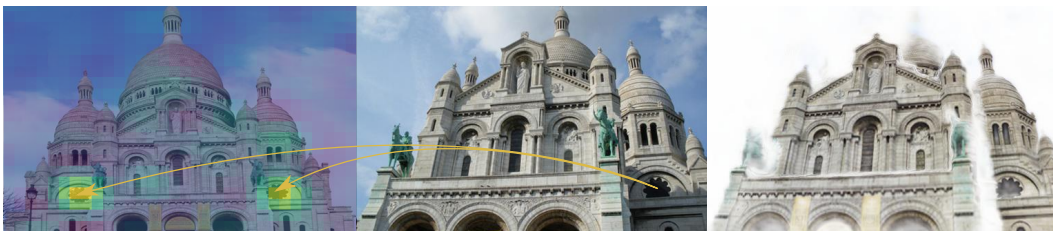


Figure 6: Example of multimodality of predicted embeddings, notably the internal embedding prediction is multimodal which is then decoded into the correct unimodal coordinate.

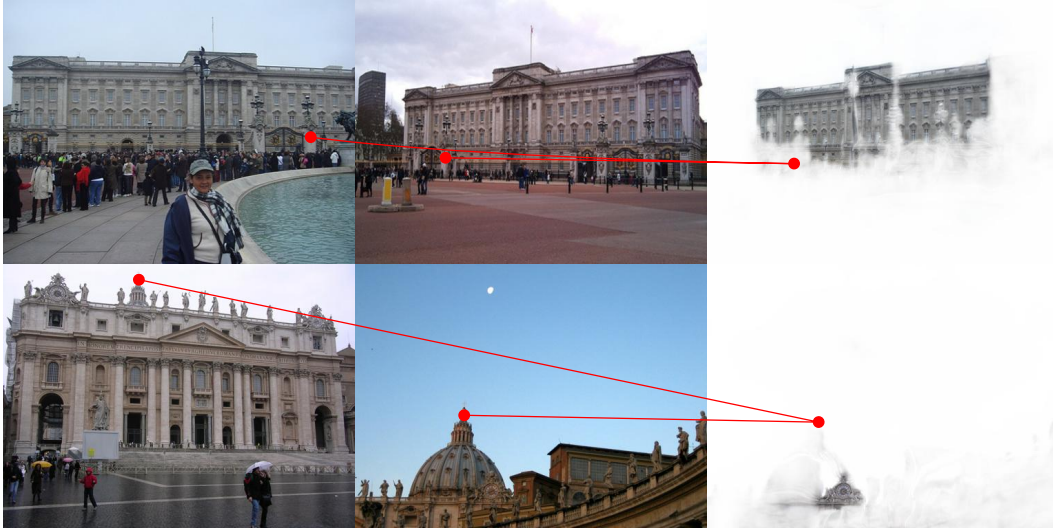


Figure 7: Figure illustrating limitations of the method. Small objects, in particular ones with significant viewpoint difference compared to larger structures, may fail to match.

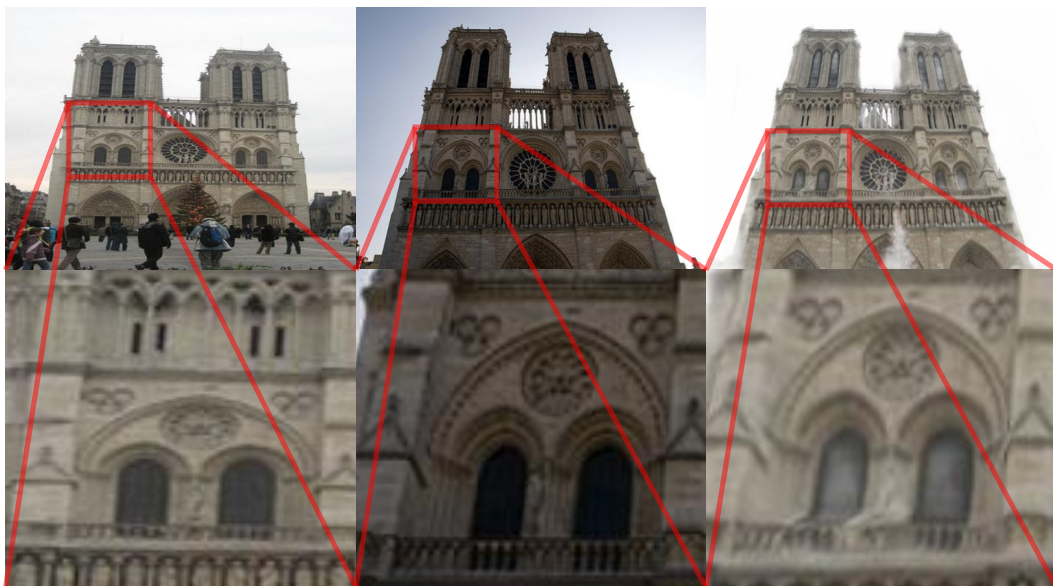


Figure 8: Figure illustrating limitations of the method. Near depth boundaries our method may occasionally give overinterpolated results, resulting in incorrect matches.

presented in Figure 6. It is clear that the network internally processes multimodal embeddings, which are decoded into a final correct unimodal prediction.

Limitations We noted two limitations of our method in the conclusion. Here we illustrate these issues with the method. The first type of failure is the model ignoring small objects, such cases are presented in Figure 7. We believe these issues are mainly caused by the first stage of global matching, where the large receptive field may be causing issues by mixing objects.

The second failure case is overinterpolation of flow near depth discontinuities. This mostly becomes an issue when the model is confident in these regions, leading to incorrect matches. We demonstrate this in Figure 8.

A.2 Metrics

PCK- τ is defined as the proportion of the correspondences between the query and support image that are less than some threshold τ away from the ground truth correspondences in the support image, *i.e.*

$$P(\|\hat{\mathbf{W}} - \mathbf{W}\|_2 < \tau). \quad (14)$$

AEPE (Average End Point Error) is defined as the *average* pixel error in the support image, and is hence quite similar to PCK. It is defined as

$$\mathbb{E}_x[\|\hat{\mathbf{W}}(x) - \mathbf{W}(x)\|_2]. \quad (15)$$

For flows we set $p(x) \propto \begin{cases} 1, & \mathbf{W}(x) \text{ is valid,} \\ 0, & \text{else.} \end{cases}$

AUC@ α is defined as the integral of precision up to α . Since the number of points is in practice finite, we follow the method by [59] and approximate the integral using the composite trapezoidal rule.

mAP@ α is defined as by [74] as the average of precision up to α , with the average only being taken on the values [5, 10, 15, 20]. This typically gives higher results than AUC, since the mAP@5 is the same as the accuracy.

Pose Error For 2-view Pose Estimation, following previous work [74] we use the pose error which is defined as the maximum angular error of both the estimated rotation and translation. The angular error of the estimated rotation is defined as

$$e_R(\hat{R}) = \left| \cos^{-1} \left(\frac{\text{tr}(R^\top \hat{R}) - 1}{2} \right) \right|, \quad (16)$$

and the angular error of the translation is the cosine similarity,

$$e_t(\hat{t}) = \frac{\langle t, \hat{t} \rangle}{\sqrt{\langle t, t \rangle \langle \hat{t}, \hat{t} \rangle}}. \quad (17)$$

With the combined error being

$$e_{R,t}(\hat{R}, \hat{t}) = \max(e_R(\hat{R}), e_t(\hat{t})). \quad (18)$$

A.3 Additional Training and Evaluation Details

MegaDepth Dataset For MegaDepth we use two different splits. For comparison with LoFTR we remove scenes 0015 and 0022 from the training set. For running YFCC100m we remove scenes 0004, 0013, 0017, and 0048. For sampling pairs we use frequency inverse weighted sampling, *i.e.*, scenes with a large number of pairs get a lower sampling weight (we use $\frac{1}{n^{0.75}}$). The final training set is composed of 2 parts, one set of pairs with minimum overlap of 0.01 and another with 0.35 (overlap is computed as fraction of covisible 3D points). This ensures that our resulting dataset has a combination of easy and difficult samples. For data augmentation we use a very simple method of random image translations with a maximum perturbation of 32 pixels.

Synthetic Dataset For the created synthetic dataset we follow PDCNet+ [58] and sample 3 independently moving objects for each generated pair. We construct the background by homographies constructed by first randomly translating the image corners uniformly up to 0.6 times half the side length, followed by an rotation of [0, 35] degrees and a scaling between [1, 1.6]. For the foreground objects we randomly rotate them by 45 degrees, followed by scaling in range [0.85, 1.25], and translation between [-0.3, 0.3] times the side length in each direction. We set the mask p to be 1 if and only if the foreground or background is covisible, *i.e.*, if an object is occluded or outside the image grid the mask is set to 0. Last, we add photometric distortion. Specifically we use the default random brightness contrast transform from Albumentations [5].

Evaluation On all benchmarks we sample 10000 matches for geometry estimation. We found estimation results to be insensitive to the exact number of matches, and hence did not optimize it further. For producing matches in original image size (*e.g.* for dense matching on HPatches) we upsample bilinearly and run the scale 1 refiner again.

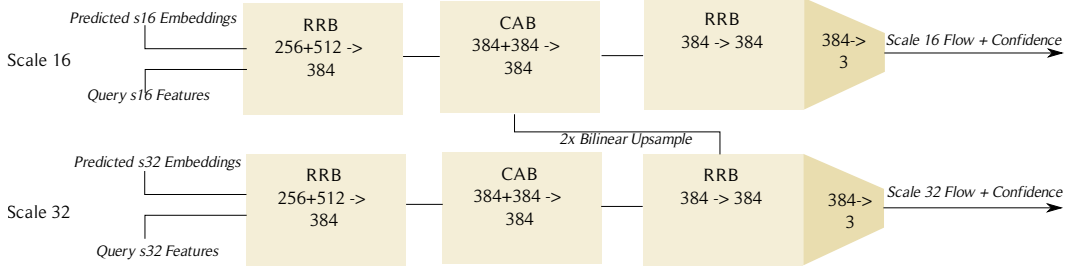


Figure 9: Overview of embedding decoder.

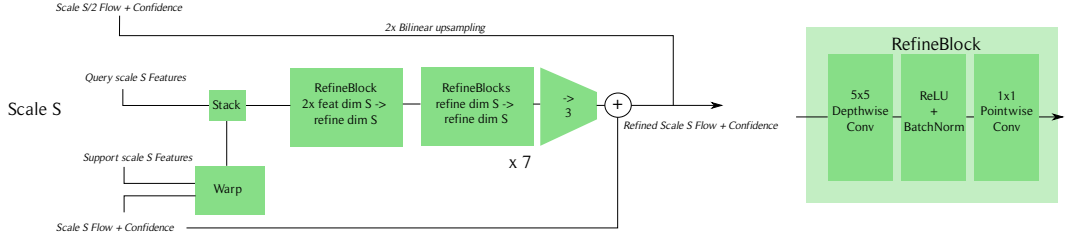


Figure 10: Overview of flow refiners.

Run Times With batch size 8, an RTX6000 GPU runs DKM inference at ~ 20 FPS. On an A100 the inference is faster, around ~ 40 FPS.

A.4 Additional Architecture Details

Coordinate Embeddings We use 256 channels for the Fourier embedding. We use a scale factor of $\ell = 8\pi$.

Embedding Decoder We use GPs on both scale 32 and 16 features of the backbone. We use an internal dimension of 384 in our decoder. The exact architecture is presented in Figure 9. The internal structure of the RRB and CAB components is described in [71].

Refiners From the decoded global flow of the decoder at scale 16 we use a set of decoders. The exact architecture is presented in Figure 10. The number of channels used at each scale is specified in Table 6.

Scale	Refinement Channels	Feature Channels
16	1024	512
8	1024	512
4	512	256
2	128	64
1	24	3

Table 6: Number of channels for each scale in refinement stage.